AJ, accepted 2006/12/1
Preprint typeset using LaTeX style emulateapj v. 10/09/06

DENSITIES OF SOLAR SYSTEM OBJECTS FROM THEIR ROTATIONAL LIGHTCURVES

Pedro Lacerda[1] and David C. Jewitt
Institute for Astronomy, University of Hawaii, 2680 Woodlawn Drive, Honolulu, HI 96822
AJ, accepted 2006/12/1

ABSTRACT

We present models of the shapes of four Kuiper belt objects (KBOs) and Jovian Trojan (624) Hektor as ellipsoidal figures of equilibrium and Roche binaries. Our simulations select those figures of equilibrium whose lightcurves best match the measured rotational data. The best fit shapes, combined with the knowledge of the spin period of the objects provide estimates of the bulk densities of these objects. We find that the lightcurves of KBOs (20000) Varuna and $2003\,EL_{61}$ are well matched by Jacobi triaxial ellipsoid models with bulk densities $992^{+86}_{-15}\,kg\,m^{-3}$ and $2551^{+115}_{-10}\,kg\,m^{-3}$, respectively. The lightcurves of (624) Hektor and KBO 2001 QG_{298} are well-described by Roche contact binary models with densities $2480^{+292}_{-80}\,kg\,m^{-3}$ and $590^{+143}_{-47}\,kg\,m^{-3}$, respectively. The nature of $2000\,GN_{171}$ remains unclear: Roche binary and Jacobi ellipsoid fits to this KBO are equivalent, but predict different densities, $\sim 2000\,kg\,m^{-3}$ and $\sim 650\,kg\,m^{-3}$, respectively. Our density estimates suggest a trend of increasing density with size.

Subject headings: Kuiper Belt objects — minor planets, asteroids — solar system: general

1. INTRODUCTION

Most small bodies of the solar system appear unresolved at the ∼0.05 arcsecond peak angular resolution offered by current technology. As a consequence, information about the shapes and rotations of the small bodies must be inferred, principally from measurements of the time dependence of the scattered radiation. So-called "lightcurve inversion" techniques have been used for decades to study the rotational properties of main-belt asteroids (Cellino et al. 1989; Kaasalainen et al. 2002). At their simplest, these involve using the peak-to-peak interval of the lightcurve to estimate the rotation period and the peak-to-peak brightness variation to estimate the "axis ratio" of bodies that are assumed to be triaxial in shape and in principal axis rotation about the minor axis. At their most complex, the inversion techniques can be used to solve for the full 3-dimensional shapes and rotation vectors, utilizing observations from a range of aspect angles (Kaasalainen & Torppa 2001; Kaasalainen et al. 2001).

All lightcurve interpretations are subject to an ambiguity between variations caused by shape and variations caused by non-uniform surface albedo, as clearly expressed a century ago by Russell (1906). This ambiguity can be broken when simultaneous optical *and* thermal observations are available, as is the case for some of the larger asteroids in the main-belt. Numerous observations of this type have shown that, with rare exceptions, the albedos of the asteroids do not vary over their surfaces by a large amount (Degewij et al. 1979). This spatial uniformity could simply mean that the compositions are intrinsically uniform. Alternatively, real surface compositional variations could exist but be smoothed-out by efficient lateral transport of dust over the surfaces of small bodies. The most famous exception to this rule is provided by Saturn's satellite Iapetus, which has a lightcurve range of nearly two magnitudes caused by surface albedo markings (Millis 1977). This case is pathological, however, in the sense that it appears to be a result of Iapetus' synchronous rotation about Saturn, which leads to unequal radiation and micrometeorite bombardment fluxes on the leading and trailing hemispheres of the satellite. This special geometric circumstance is presumably not relevant to the case of small bodies in heliocentric orbit.

In the outer solar system, lower temperatures and greater distances make the detection of thermal radiation increasingly challenging, even with the most sensitive infrared satellites in space (e.g. Cruikshank 2005). Consequently, only the reflected lightcurve is available, and the interpretation must be based on the *assumption* that the surface albedo variation is minimal. As we will see, support for this assumption comes not only from the analogy with the (generally uniform) main-belt asteroids, but from the remarkably symmetric lightcurves displayed by most outer solar system objects. Rotational symmetry is expected for figures of equilibrium having uniform surface albedos but is not a natural consequence of surface albedo markings.

The lightcurves of several large Kuiper Belt Objects (KBOs), notably (20000) Varuna (Jewitt & Sheppard 2002) and 2003 EL61 (Rabinowitz et al. 2006), suggest that these are high-angular momentum bodies in which the shape has been deformed by rapid rotation. Other objects may be contact binary systems, as has long been suggested for Jovian Trojan (624) Hektor (Hartmann & Cruikshank 1978, 1980; Weidenschilling 1980) and, recently, for KBO 2001 QG_{298} (Sheppard & Jewitt 2004; Takahashi & Ip 2004). These systems are interesting since, under conditions of rotational equilibrium, the period and the shape (both of which can be inferred from lightcurve data) are uniquely related to the bulk density. Lightcurves of these objects may thus be interpreted in terms of a fundamental geophysical property that is otherwise difficult to measure.

In this paper, we discuss the lightcurves of specific solar

Electronic address: pedro@ifa.hawaii.edu,jewitt@ifa.hawaii.edu
[1] GAUC, Departamento de Matemática, Lg. D. Dinis, 3000 Coimbra, Portugal

TABLE 1
(624) Hektor lightcurve data.

JD [a]	θ [b] [deg]	α [c] [deg]	$\Delta m_{\rm data}$ [d] [mag]	$\Delta m_{\rm model}$ [e] [mag]
JD2435989	74.9	+4.4	0.775	0.737
JD2438795	24.8	+4.1	0.113	0.063
JD2439556	52.5	−5.3	0.398	0.302
JD2439977	86.3	+4.1	1.055	1.048

Note. — Sources cited in Section 3.1.
[a] Date of observation[b] Aspect angle[c] Phase angle[d] Data lightcurve range[e] Best-fit model lightcurve range

TABLE 2
List of objects to fit.

Object [a]	Family [b]	H [mag] [c]	$D_{\rm e}$ [km] [d]	P [hr] [e]	Δm [mag] [f]	ρ [$\mathrm{kg\,m^{-3}}$] [g]
Triaxial ellipsoids						
$2003\,\mathrm{EL}_{61}$	KBO	0.2	1450	3.9154	0.28 ± 0.04	2585^{+81}_{-44}
Varuna	KBO	3.2	900	6.3442	0.42 ± 0.02	992^{+86}_{-15}
$2000\,\mathrm{GN}_{171}$	KBO	6.0	360	8.329	0.61 ± 0.03	1946^{+1380}_{-344}
Roche binaries						
$2001\,\mathrm{QG}_{298}$	KBO	6.9	240	13.7744	1.14 ± 0.04	590^{+143}_{-47}
$2000\,\mathrm{GN}_{171}$	KBO	6.0	360	8.329	0.61 ± 0.03	650^{+75}_{-80}
(624) Hektor	Trojan	7.5	180	6.9225	1.2 [h]	2480^{+80}_{-292}

Note. — Sources cited in the text. KBO $2000\,\mathrm{GN}_{171}$ is intentionally listed twice, as its nature is uncertain.
[a] Object designation.[b] Object family.[c] Absolute magnitude.[d] Approximate equivalent circular diameter.[e] Rotation period.[f] Peak-to-peak lightcurve range.[g] Estimated density.[h] Maximum predicted amplitude, at $\theta = 90\,\mathrm{deg}$.

system bodies in terms of rotational equilibrium models, paying particular attention to high angular momentum systems and contact binaries. Our models address the effects of the surface scattering on the derived system parameters. Prototype contact binary (624) Hektor is examined in detail, taking advantage of voluminous high quality data published for this object over a range of aspect angles (see Table 1). The models are then applied to four well-observed KBOs (Table 2) and used to place quantitative contraints on their properties in a consistent formalism. Indeed, the uniformity of approach is one of the strengths of our simulations.

2. LIGHTCURVE SIMULATIONS

2.1. *Jacobi Ellipsoids*

The formalism associated with the ellipsoidal figures of equilibrium is described in great detail in Chandrasekhar (1969). A homogeneous, fluid body spinning in free space will assume a shape that balances self-gravity and the inertial acceleration due to rotation. This means that the triaxial shape of such a body is a function of its spin frequency and density. The equilibrium figures of isolated, rotating bodies are the Maclaurin spheroids and the Jacobi ellipsoids. The former are oblate spheroids and the latter are triaxial ellipsoids, and in both cases the rotation is about the shortest physical axis. We are interested only in the Jacobi ellipsoids because oblate spheroids have rotational symmetry and thus produce flat lightcurves.

The shapes of Jacobi ellipsoids in terms of the semi-axes (a, b, c) can be obtained by solving (Chandrasekhar 1969)

$$a^2 b^2 \int_0^\infty \frac{1}{(a^2+u)\,(b^2+u)\;\Delta(a,b,c)}\,du = c^2 \int_0^\infty \frac{1}{(c^2+u)\;\Delta(a,b,c)}\,du \qquad (1)$$

where $\Delta(a,b,c) = \sqrt{(a^2+u)\,(b^2+u)\,(c^2+u)}$. The spin frequency ω and density ρ are related to the shape by

$$\frac{\omega^2}{\pi\,G\,\rho} = 2\,a\,b\,c \int_0^\infty \frac{u}{(a^2+u)\,(b^2+u)}\,du \qquad (2)$$

where G is the gravitational constant. We solved Eq. (2) for values of b/a between 0.43 and 1.00 in steps of 0.01, and used the solutions, together with Eq. (2), to calculate $\omega^2/(\pi\,G\,\rho)$ which relates the spin period to the body density for each of the equilibrium triaxial ellipsoids. Figures with $b/a < 0.43$ are unstable to rotational fission (Jeans 1919).

The derived shapes are then raytraced at regular intervals spanning a full rotation period. This produces a set of frames from which the lightcurve is extracted by integrating the total light in each one of them. In this way we generate a database of lightcurves of figures of equilibrium which can be used to compare to the lightcurve

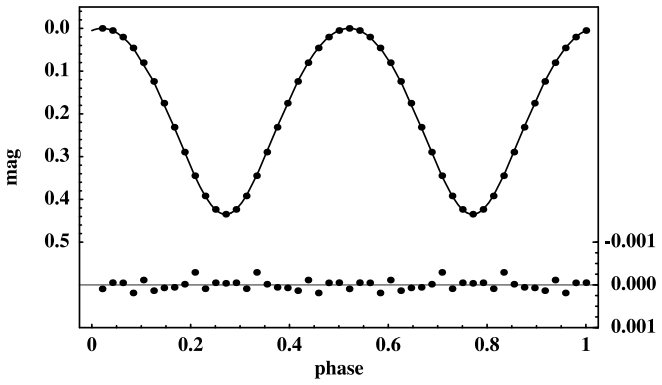

FIG. 1.— Accuracy of raytraced versus analytical solution, for an ellipsoid with a "lunar" type surface, an axis ratio b/a=2/3, observed at aspect angle $\theta = 90°$ and phase angle $\alpha = 0°$. Bottom points and right ordinate axis show difference between the points (raytraced) and the line (analytical) shown at the top.

data. As described below we run our simulations for two surface scattering laws.

The raytracing is done using the main engine of the open source software POV-Ray (http://www.povray.org). The surface scattering routines were rewritten to permit accurate control of the scattering function. To test the accuracy of our raytracing method we simulated the lightcurve of a triaxial ellipsoid with an axis ratio b/a, observed equator-on ($\theta = 0°$) at zero phase angle ($\alpha = 0°$), using a "lunar" surface scattering function (see Section 2.3), and compared the result with the analytical solution for the same configuration, given by

$$m(b/a, \phi) = 2.5 \log_{10} \sqrt{1 + [(b/a)^2 - 1] \cos^2(2\,\pi\,\phi)}. \quad (3)$$

where $\phi \in [0, 1]$ is the rotational phase of the ellipsoid. The result is plotted in Fig. 1. The raytraced lightcurve deviates $\sim 0.1\%$ from the analytical solution which is negligible when compared to the uncertainties in the photometric data, typically ~ 2 to 3% on real astronomical objects.

2.2. *Roche Binaries*

Lightcurves from an eclipsing binary asteroid consisting of two spheres in circular orbit have been presented by Wijesinghe & Tedesco (1979). As the binary separation becomes comparable to the scale of either component, mutual gravitational forces will deform the bodies, increasing the lightcurve range over the maximum (factor of two) possible for equal-sized spheres (Leone et al. 1984). To model this mutual deformation in close and contact binary systems we use the Roche binary approximation (Chandrasekhar 1963; Leone et al. 1984). In this approximation each component is considered to be a Roche ellipsoid, which is the equillibrium shape of a satellite orbiting a spherical, more massive primary. The tidally deformed shape of the secondary is assumed to be solely caused by the spherically symmetric gravitational gradient due to the primary. Each component's shape is calculated separately using reciprocal values, q and $1/q$, for the mass ratio. Clearly, such an approximation introduces the most error when calculating shapes of close binaries with mass ratios near $q = 1$. In these situations the elongation of the binary components is underestimated which leads to smaller lightcurve ranges. With the further assumptions that the binary is tidally locked, and that the components have equal density ρ, and orbit the center mass in circular paths, the mass ratio q, the shape of one of the components $(b/a, c/a)$, and the orbital frequency ω can be calculated by solving (Chandrasekhar 1963)

$$\frac{(3 + 1/q)\,a^2 + c^2}{(1/q)\,b^2 + c^2} = \frac{a^2 A_1 - c^2 A_3}{b^2 A_2 - c^2 A_3} \quad (4a)$$

$$\frac{q}{1+q}\,\frac{\omega^2}{\pi\,G\,\rho} = 2\,a\,b\,c\,\frac{a^2 A_1 - c^2 A_3}{(3 + 1/q)\,a^2 + c^2}, \quad (4b)$$

with A_1, A_2, and A_3 given by (Chandrasekhar & Lebovitz 1962)

$$A_1 = \frac{2}{a^3 \sin^3\phi}\,\frac{1}{\sin^2\theta}\,[F(\theta,\phi) - E(\theta,\phi)] \quad (5a)$$

$$A_2 = \frac{2}{a^3 \sin^3\phi}\,\frac{1}{\sin^2\theta\cos^2\theta}\times \quad (5b)$$
$$\left[E(\theta,\phi) - F(\theta,\phi)\cos^2\theta - \left(\frac{c}{b}\right)\sin^2\theta\sin\phi\right]$$

$$A_3 = \frac{2}{a^3 \sin^3\phi}\,\frac{1}{\cos^2\theta}\left[\left(\frac{b}{c}\right)\sin\phi - E(\theta,\phi)\right], \quad (5c)$$

where $E(\theta,\phi)$ and $F(\theta,\phi)$ are the standard elliptic integrals of the two kinds with arguments

$$\theta = \arcsin\sqrt{\frac{a^2 - b^2}{a^2 - c^2}} \quad \text{and} \quad \phi = \arccos\left(\frac{c}{a}\right). \quad (6)$$

Each root of Eq.(4a), corresponding to a Roche ellipsoid solution, can be calculated by setting 3 of the 4 parameters q and (a, b, c), and solving for the 4th by interpolation. For the primary, we set $a = 1$ and calculate b for each combination of $q = q_{\min}, \ldots, 1.00$ and $c = c_{\min}, \ldots, 0.99$, both in steps of 0.01. The procedure is repeated using $1/q$ instead of q to calculate the shape of the secondary, (a', b', c'). A valid Roche binary solution is obtained if two sets, (q, a, b, c) and $(1/q, a', b', c')$, yield the same value $\omega^2(\pi\,G\,\rho)^{-1}$ when replaced into the right-hand side of Eq.(4b). Table 3 shows the solutions for $q = 0.25$.

2.3. *Surface Scattering*

The surface scattering properties of KBOs are unknown. For this reason the amount of sunlight reflected from a KBO is usually taken to be proportional to its geometrical cross-section. However, the total range of the lightcurve of a convex object increases significantly if there is limb darkening. The two simplest scattering laws generally used to model planetary surfaces are the Lommel-Seeliger and Lambert laws. The Lommel-Seeliger law is a single scattering model, suitable for low albedo surfaces, and can be considered a simplification of the well known Hapke model (Li 2005). The Hapke model is inappropriate for this work because it has many parameters which cannot realistically be constrained using lightcurve data. To model relative brightness variations, which is what is needed to generate lightcurves, the Lommel-Seeliger law requires no parameters: it depends solely on the cosines of the incidence and emission angles (i and e, the angles between the surface normal and the directions to the light source and to the observer). The Lommel-Seeliger reflectance function is thus

$$r_{\rm LS} \propto \frac{\mu_0}{\mu + \mu_0} \quad (7)$$

TABLE 3
ROCHE BINARY SOLUTIONS FOR MASS RATIO $q = 0.25$.

q [a]	B/A [b]	C/A [b]	b/a [c]	c/a [c]	$\omega^2/(\pi G \rho)$ [d]	l [e]
0.25000	0.91674	0.83000	0.51426	0.48000	0.10626	1.19222
0.25000	0.92292	0.84000	0.61175	0.57000	0.10137	1.28193
0.25000	0.92891	0.85000	0.66433	0.62000	0.09554	1.34473
0.25000	0.93473	0.86000	0.70532	0.66000	0.08945	1.40392
0.25000	0.94037	0.87000	0.73534	0.69000	0.08368	1.45810
0.25000	0.94584	0.88000	0.76469	0.72000	0.07755	1.51789
0.25000	0.95114	0.89000	0.79333	0.75000	0.07109	1.58466
0.25000	0.95629	0.90000	0.81200	0.77000	0.06558	1.64436
0.25000	0.96128	0.91000	0.83935	0.80000	0.05864	1.72902
0.25000	0.96612	0.92000	0.85713	0.82000	0.05282	1.80713
0.25000	0.97081	0.93000	0.88311	0.85000	0.04550	1.92216
0.25000	0.97537	0.94000	0.89996	0.87000	0.03943	2.03365
0.25000	0.97979	0.95000	0.91642	0.89000	0.03328	2.17018
0.25000	0.98407	0.96000	0.93250	0.91000	0.02706	2.34450
0.25000	0.98824	0.97000	0.95588	0.94000	0.01924	2.65422

[a] Mass ratio[b] Primary axes ratios[c] Secondary axes ratios[d] Orbital frequency squared in units of $\pi G \rho$, where G is the gravitational constant[e] Orbital distance in units of $A + a$

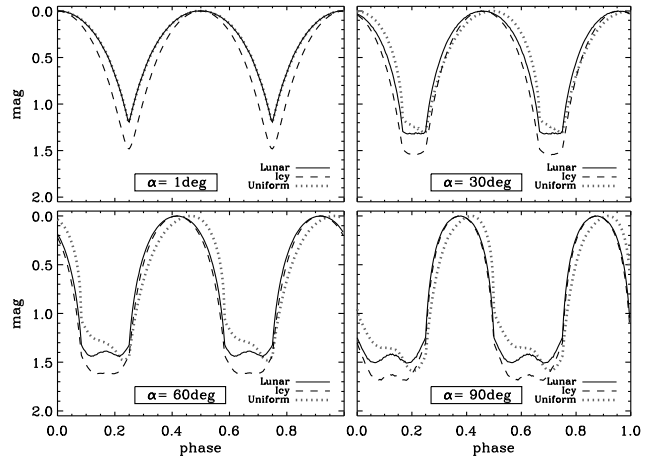

FIG. 2.— Lightcurves of a Roche contact binary at different phase angles and for different scattering laws. In the "uniform" case every point of the surface that is illuminated by sunlight reflects exactly the same amount of light back to the observer. Both primary and secondary have axis ratios $b/a = 0.67$ and $c/a = 0.60$, and the components are in contact.

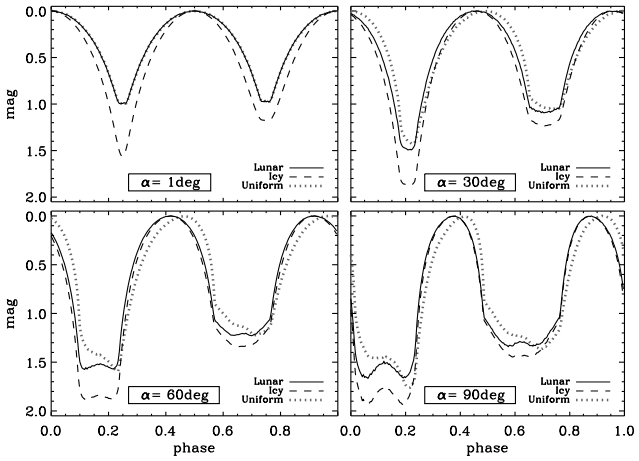

FIG. 3.— Same as Fig. 2 but for a binary with different size components. Mass ratio is $q = 0.67$ and the components have axis ratios $(B/A = 0.77, C/A = 0.69)$ and $(b/a = 0.53, c/a = 0.49)$.

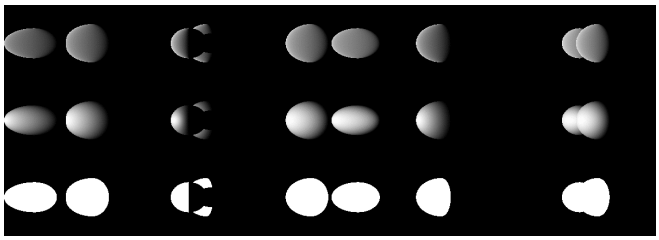

FIG. 4.— Three-dimensional rendering of the binary used to produce Fig. 3 ($\alpha = 60$ deg). Rotational phase ($\phi = 0, 72, 144, 216,$ and 288 deg) runs from left to right and top to bottom rows show lunar, icy, and uniform surface scattering functions.

where $\mu_0 = \cos i$ and $\mu = \cos e$.

The Lambert scattering law is a simple description of a perfectly diffuse surface. It assumes that a light ray that enters the material is multiply scattered and thus leaves the surface in a random direction. As such, it is a multiple scattering law which adequately describes high albedo surfaces. The Lambert reflectance function is

$$r_{\rm L} \propto \mu_0. \qquad (8)$$

The Lommel-Seeliger and Lambert scattering functions are taken here as representative of low albedo "lunar"-type surfaces and high albedo "icy"-type surfaces, respectively.

Figures 2 and 3 compare the lightcurves of Roche contact binaries using both lunar and icy scattering models, at four different phase angles. A "uniform" scattering law is also plotted for comparison. The uniform model assigns equal brightness to any illuminated point on the surface, and thus represents the illuminated cross-section. Figure 2 is for a contact binary with equal size components, while Fig. 3 represents the case of different sizes for primary and secondary (see Fig. 3). A few conclusions can immediately be drawn from inspection of Figs. 2 and 3:

- At low phase angle the lunar model produces negligible limb darkening and is thus equivalent to the simpler uniform model. Only at large phase angles ($\gtrsim 30$ deg) does the uniform approximation fail to follow the lunar scattering law. Icy surfaces, however, always produce larger lightcurve ranges for the same shape, which implies that assuming uniform scattering when interpreting lightcurves of icy objects will tend to exaggerate the inferred shape

elongation.

- The lightcurve minima become broader with increasing phase angle. This fact implies that V-shaped minima are strictly diagnostic of a close binary configuration only when viewed near zero phase angle. Fortunately, this is necessarily the case for all observations of Kuiper belt objects.

- Observations at different phase angles shift the minima and maxima of the lightcurve in rotational phase. This effect should be taken into account when fitting a single spin period to observations taken at different phase angles. For instance, failure to fit all the data with a single period does not necessarily imply complex (non-principal axis) rotation when observations over a wide range of phase angles are compared.

In our simulations we use the lunar- and icy-type surface laws separately to assess how different surface properties affect our results. As shown below, we find that different surface properties do not significantly change our density estimates. It is also shown that while in some cases the choice of a particular scattering law clearly improves the lightcurve fit, in other cases the result is degenerate as far as surface properties are concerned. The simulations further assume that the surface albedo is uniform and the same for both components of the binary.

2.4. *Observational Geometry*

Owing to their large distances from the Sun and the Earth, KBOs can only be observed at small phase angles ($\alpha < 2\,\mathrm{deg}$). (20000) Varuna is known to exhibit a pronounced opposition effect at phase angle $\alpha < 0.1\,\mathrm{deg}$ (Hicks et al. 2005) which seems to affect the extent of its brightness variation (Belskaya et al. 2006). In the range $0.1\,\mathrm{deg} < \alpha < 2.0\,\mathrm{deg}$ the phase curve of (20000) Varuna is linear (Sheppard & Jewitt 2002) and the lightcurve unnaffected by phase effects. We place our simulations well within this linear regime by using a phase angle $\alpha = 1\,\mathrm{deg}$. In addition, since most of the data being modeled have $\alpha > 0.1\,\mathrm{deg}$ the opposition effect is likely unimportant to the conclusions presented here.

The aspect angle is the angle between the line-of-sight and the spin axis of the system. We simulated lightcurves for two values of the aspect angle: 90 degrees (equator-on) and 75 degrees. Given that the spin axis orientations are unknown, the models with a tilted orientation allow us to investigate how the aspect angle affects our conclusions. In the case of (624) Hektor the spin (orbital) axis orientation is known (Dunlap & Gehrels 1969) and we were able to perform simulations using the actual aspect and phase angles at the moment the data were taken (see Table 1).

3. BEST FIT SOLUTIONS

3.1. *(624) Hektor*

Jovian Trojan (624) Hektor has long been recognized as a likely contact binary (Hartmann & Cruikshank 1978, 1980; Weidenschilling 1980). Numerous lightcurve data spanning a long time base (1957–1968) have been collected for this object, which allowed the determination of the pole orientation (Dunlap & Gehrels 1969; de Angelis 1995). Depending on the orbital configuration, the lightcurve range of (624) Hektor varies between 0.1 mag and 1.2 mag (see Table 1). As noted by Weidenschilling (1980, see also Leone et al. 1984), lightcurve ranges above 0.9 mag cannot be produced by rotation of a single equilibrium figure and, instead, are most likely produced by a tidally distorted contact binary. Besides the large range of variability, the lightcurve morphology of (624) Hektor exhibits V-shaped minima and round maxima, also characteristic of tidally deformed, contact binary systems.

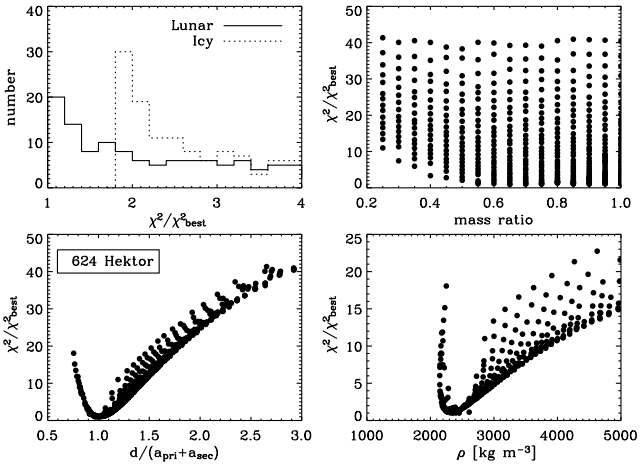

FIG. 5.— Quality of fit as a function of scattering function (top-left), mass ratio of binary components (top-right), orbital distance (bottom-left), and bulk density of binary components (bottom-right) for (624) Hektor. To avoid cluttering, only Roche models with mass ratio values, q, multiple of 0.05 are plotted.

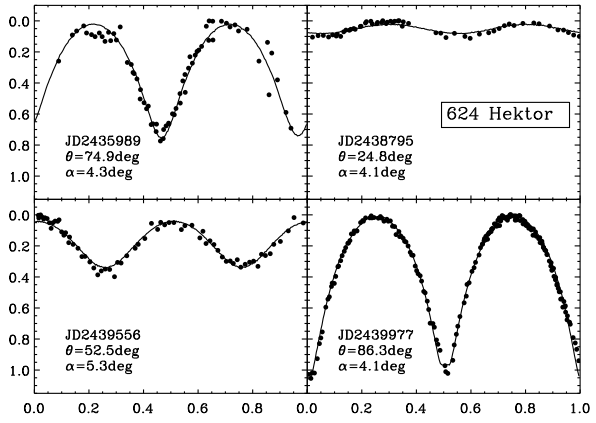

FIG. 6.— Roche binary model lightcurve superimposed on data for (624) Hektor taken at 4 different aspects.

Making use of the extensive dataset presented in Dunlap & Gehrels (1969), we have selected the Roche binary model (see Section 2.2) that simultaneously best fits the observations at four observing campaigns (see Table 1). The quality of fit is measured by $\chi^2/\chi^2_{\mathrm{best}}$, i.e., the ratio of the chi-squared value of each model to the chi-squared value of the best fit model. This corresponds to a reduced chi-squared, χ^2_{red}, if one assumes that the best fit model has $\chi^2_{\mathrm{red}} = 1$. We do this because the errors associated with the data for (624) Hektor are not known with certainty, which does not allow us to reliably calculate the reduced chi-squared for each model. In Table 4

TABLE 4
Best three Roche binary model fits to (624) Hektor.

SL [a]	q [b]	B/A [c]	C/A [c]	b/a [d]	c/a [d]	$\omega^2/(\pi G \rho)$ [e]	$d/(A+a)$ [f]	ρ [g]	$\chi^2/\chi^2_{\rm best}$ [h]
Lunar	0.62	0.80	0.72	0.47	0.43	0.122	0.98	2480	1.00
Lunar	0.67	0.77	0.69	0.53	0.49	0.128	1.00	2374	1.06
Lunar	0.65	0.79	0.71	0.47	0.43	0.124	0.97	2453	1.08

[a] Surface type. [b] Mass ratio of the binary components. [c] Axis ratios of primary. [d] Axis ratios of the secondary [e] Orbital frequency of binary. [f] Binary orbital separation. [g] Bulk density of the bodies (in $\mathrm{kg\,m^{-3}}$). [h] Ratio of χ^2 of model to χ^2 of best-fit model.

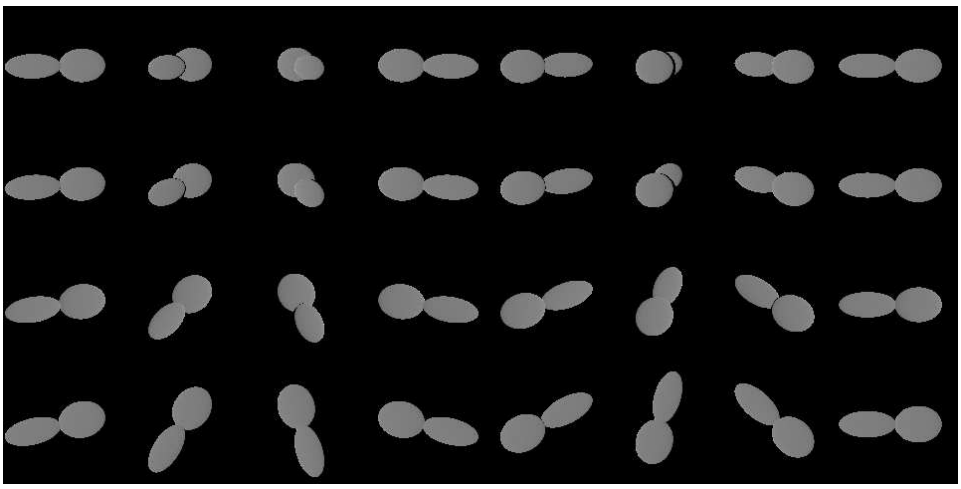

Fig. 7.— Rendering of best-fit Roche binary model for (624) Hektor for the 4 geometries listed in Table 1. Rotational phase (ϕ = 15, 60, 105, 165, 210, 255, 315, and 360 deg) runs from left to right while aspect angle decreases from top to bottom.

we show the three Roche models that best approximate (624) Hektor's lightcurve. Figure 5 shows how well our simulations are able to determine the density, orbital distance, mass ratio, and surface scattering properties of the (624) Hektor system. In the upper left panel we plot histograms of quality of fit for the two scattering laws considered. A lunar scattering law clearly produces better fits, which is no surprise as (624) Hektor is known to have a low albedo (∼0.06, Cruikshank 1977; Fernández et al. 2003). In the lower left panel the orbital distance of the Roche binary models is plotted versus quality of fit. The orbital distance is given in units of the sum of the semi-major axes of the primary, A, and of the secondary, a. The minimum is centered around $d/(A+a) = 1$, which corresponds to the binary components being in contact. Values $d/(A+a) < 1$ are unphysical but we have decided to keep them for two reasons. Firstly, because they may result from the approximations of the Roche model (Leone et al. 1984). The orbital distance is calculated using Kepler's 3rd law assuming point masses for the binary components. Since these have elongated shapes, gravity will be enhanced meaning the Roche model may underestimate the orbital distance. Secondly, because the mechanism that brought the two components together and formed the binary may have produced some deformation (a "crush" zone) around the point of contact, bringing the objects closer together than the situation of contact between two perfectly hard ellipsoids. Considering models with $\chi^2/\chi^2_{\rm best} < 2$, which roughly corresponds to a 1-σ criterion, we find that the two components of (624) Hektor are separated by $d/(A+a) = 1.00^{+0.11}_{-0.09}$, which is consistent with contact. The top right panel of Fig. 5 shows that the model poorly constrains the mass ratio of the binary. The mass ratio which corresponds to the best fit Roche binary is $q = 0.62$, but the range of q values that fall within 1-σ of the best fit is broad. As for the bulk density of (624) Hektor (bottom right panel of Fig. 5), perhaps the most interesting quantity to come out of our simulations, we find $\rho = 2480^{+80}_{-292}\,\mathrm{kg\,m^{-3}}$. This value closely confirms an earlier estimate: $\rho \sim 2500\,\mathrm{kg\,m^{-3}}$ (Weidenschilling 1980).

Figure 6 shows how the best Roche binary model compares to the Dunlap & Gehrels (1969) lightcurve data. The differences in lightcurve range from one campaign to the next reflect the effect of the observational geometry. Given the simplicity of the model, the agreement is remarkable and lends strong support to the idea that (624) Hektor is a contact binary. The model for Julian day 2438795 shows the largest departure from the data. This is to be expected given the small aspect angle, $\theta = 24.8$ deg. The cross-section of the binary varies little at such unfavorable geometry and brightness variations must be attributed to irregularities on the surface of the Trojan, which are not accounted for in the model. In Fig. 7 we show the best fit model rendered at the four aspect angles and for eight values of rotational phase. Recent observations using the LGS AO system at the Keck-II telescope suggest that (624) Hektor may have a bilobated shape (Marchis et al. 2006b) and lend further support to the results presented here.

3.2. *2001 QG_{298}*

Kuiper belt object $2001\,\mathrm{QG_{298}}$ completes a full rotation every $P = 13.77$ hr and its brightness varies by $\Delta m = 1.14 \pm 0.04$ mag (Sheppard & Jewitt 2004). The large range of brightness variation and relatively slow ro-

TABLE 5
$2001\,QG_{298}$ MODEL FIT.

S.F. [a]	θ [b]	q [c]	B/A [d]	C/A [d]	b/a [e]	c/a [e]	$\omega^2/(\pi G \rho)$ [f]	$d/(A+a)$ [g]	ρ [h]	$\chi^2/\chi^2_{\rm best}$ [i]
Jacobi ellipsoid										
Lunar	90	-	0.43	0.34	-	-	0.283	-	271	2.21
Icy	90	-	0.56	0.41	-	-	0.327	-	234	2.50
Lunar	75	-	0.43	0.34	-	-	0.283	-	271	6.60
Icy	75	-	0.50	0.38	-	-	0.310	-	248	2.51
Roche binary										
Lunar	90	0.84	0.72	0.65	0.45	0.41	0.130	0.90	590	1.00
Icy	90	0.44	0.85	0.77	0.53	0.49	0.116	1.09	659	1.09
Lunar	75	1.00	0.44	0.40	0.44	0.40	0.135	0.76	568	1.62
Icy	75	0.73	0.74	0.67	0.54	0.49	0.130	0.98	589	1.16

[a] Surface type. [b] Aspect angle. [c] Mass ratio of the binary components. [d] Axis ratios of primary. [e] Axis ratios of the secondary [f] Spin (orbital) frequency of triaxial ellipsoid (binary). [g] Binary orbital separation. [h] Bulk density of the bodies (in $\mathrm{kg\,m^{-3}}$). [i] Ratio of χ^2 of model to χ^2 of best-fit model.

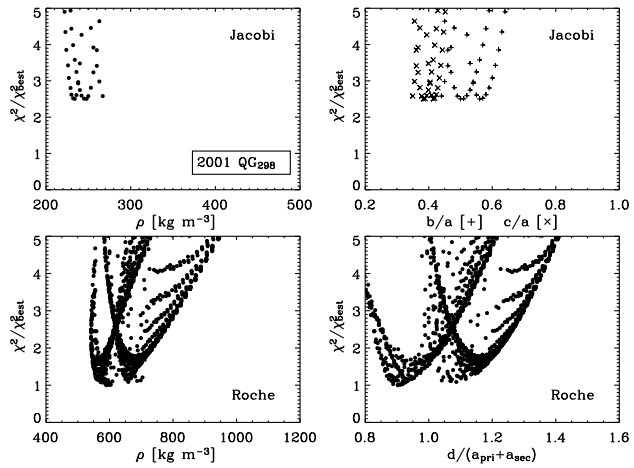

FIG. 8.— Quality of fit versus bulk density (top-left) and axis ratios (top-right) of Jacobi ellipsoid models, and versus bulk density (bottom-left) and orbital distance (bottom-right) of Roche binary models for $2001\,QG_{298}$ lightcurve data. Jacobi ellipsoid models are plotted for all four combinations of surface properties and observational geometry listed in Table 5, while Roche binary models are plotted for both lunar- and icy-type surfaces at an aspect angle $\theta = 90°$.

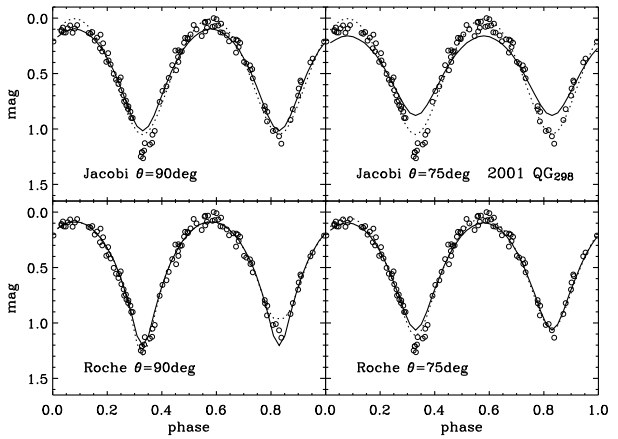

FIG. 9.— Models that best fit the lightcurve of $2001\,QG_{298}$ for each combination of scattering law and geometry. Solid and dotted lines indicate lunar and icy surface scattering models, respectively.

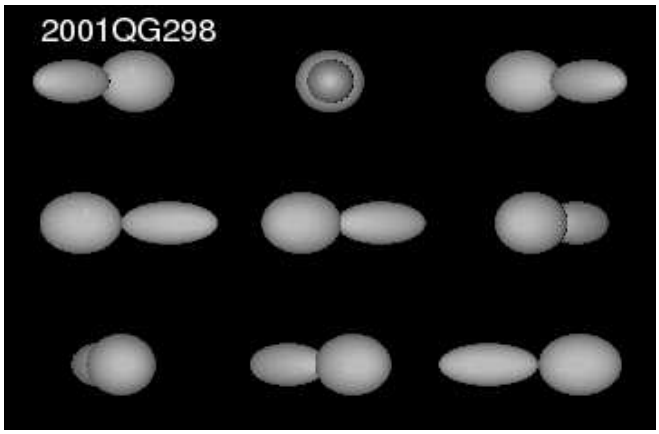

FIG. 10.— Rendering of best-fit Roche binary model for $2001\,QG_{298}$. Rotational phase ($\phi = 45, 90, 135, 165, 210, 240, 285, 315,$ and $360\,\mathrm{deg}$) runs from left to right and top to bottom.

tation provide compelling evidence that $2001\,QG_{298}$ is a contact or very close binary (Sheppard & Jewitt 2004). We attempted to fit both Jacobi ellipsoid and Roche binary models to the lightcurve data on $2001\,QG_{298}$, using the two surface scattering laws and the two different observational geometries described in Sections 2.3 and 2.4. Table 5 and Figures 8 and 9 present a summary of the best fit models for different combinations of scattering law and observational geometry.

Clearly, the Roche binary simulations fit the data better. Furthermore, the binary model favored by the data has a lunar-type surface and an equator-on geometry (see Fig. 9). However, choosing an icy-type surface does not result in a significantly poorer fit. Indeed, the lower left panel of Fig. 9 suggests that an intermediate scattering law is needed to fit the shallower minimum in the lightcurve data. Models tilted 15 degrees toward the line of sight are unable to fit the deeper V-shaped minimum in the data. Taking all the Roche simulations into account we find that $2001\,QG_{298}$ should have an orbital separation $d/(A+a) = 0.90^{+0.31}_{-0.14}$ (contact binary) and a bulk density $\rho = 590^{+143}_{-47}\,\mathrm{kg\,m^{-3}}$. The uncertainty intervals are established in the same way as was done for

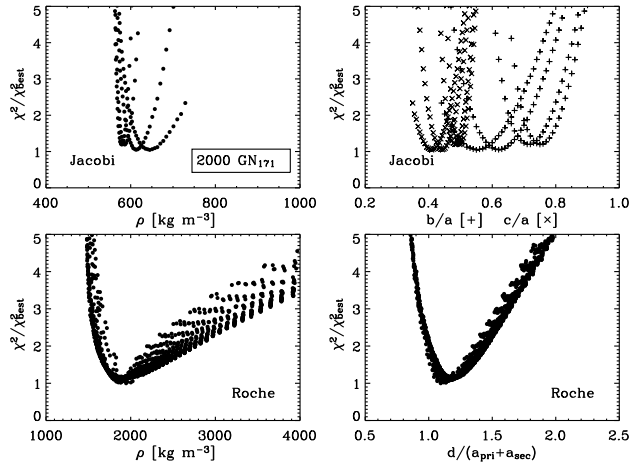

FIG. 11.— Same as Fig. 8 but for $2000\,GN_{171}$ lightcurve data. Jacobi ellipsoid models are plotted for all four combinations of surface properties and observational geometry listed in Table 6, while Roche binary models are plotted for lunar-type surface and aspect angle $\theta = 75°$.

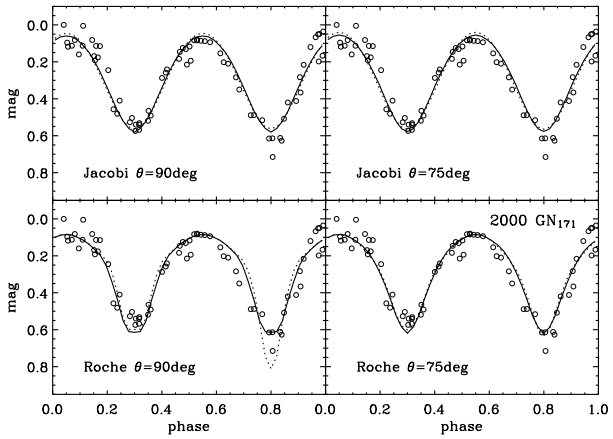

FIG. 12.— Same as Fig. 9 but for $2000\,GN_{171}$.

(624) Hektor (see Section 3.1). Inspection of Table 5 and Fig. 8 shows that the best icy-type surface models have $d \sim 1.09$ and $\rho \sim 660\,\mathrm{kg\,m^{-3}}$. Given that the chosen surface scattering laws represent extreme cases (the surface of 2001 QG_{298} probably combines single and multiple scattering behaviour), we must conclude that the density we find does not depend strongly on the specific surface scattering properties of the KBO. The same applies to the binary components being in (or very close to) contact. The best fit Roche binary is rendered in Fig. 10. Our results are in good agreement with an independent but similar attempt to fit this object's lightcurve with a Roche binary model (Takahashi & Ip 2004).

3.3. *2000 GN_{171}*

The rotational properties of KBO $2000\,GN_{171}$ also make it a good candidate contact binary (Sheppard & Jewitt 2004). Its spin period and lightcurve range are $P = 8.329\,\mathrm{hr}$ and $\Delta m = 0.61 \pm 0.03\,\mathrm{mag}$ (Sheppard & Jewitt 2002). However, as can be seen in Table 6 and Figures 11 and 12, the lightcurve fitting results are not definitive about the nature of this KBO. A Roche binary solution is the one that best fits the data

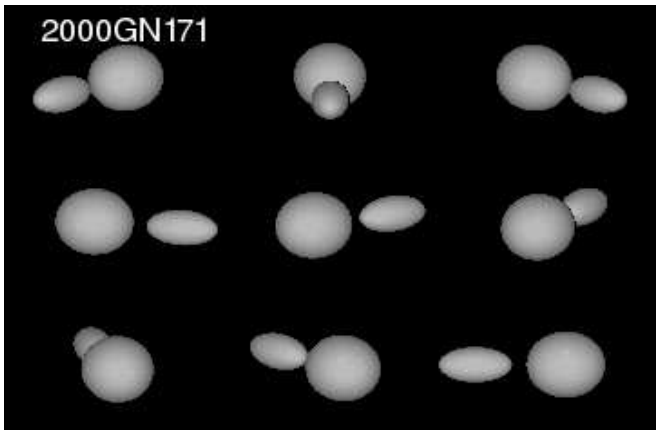

FIG. 13.— Same as Fig. 10 but for $2000\,GN_{171}$.

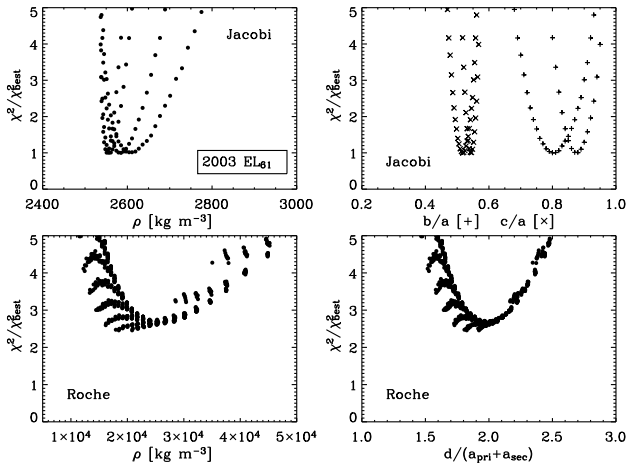

FIG. 14.— Same as Fig. 8 but for $2003\,EL_{61}$ lightcurve data. Jacobi ellipsoid models are plotted for all four combinations of surface properties and observational geometry listed in Table 7, while Roche binary models are plotted for icy-type surface at an aspect angle $\theta = 75°$.

(see Table 6) but it is not significantly better than a single Jacobi ellipsoid model. Inspection of the lightcurve fits (Fig. 12) suggests that while the Jacobi ellipsoid model follows better the overall shape of the lightcurve, it is not able to reproduce the different minima present in the data. A Roche binary solution produces different minima, but seems to require an aspect angle $\theta < 90\,\mathrm{deg}$ and a low mass ratio ($q \sim 0.3$) to be able to reproduce a lightcurve range as low as $\Delta m = 0.61\,\mathrm{mag}$. The predicted orbital separation is $d/(A+a) = 1.09^{+0.55}_{-0.10}$. Lunar-type surface models consistently produce better fits than icy-type, irrespective of the nature (Jacobi ellipsoid or Roche binary) and orientation of $2000\,GN_{171}$. The inferred density is model dependent, but for each of the two models it does not depend much on scattering properties nor on geometry. If $2000\,GN_{171}$ is taken to be a binary, its density should be $\rho \sim 2000\,\mathrm{kg\,m^{-3}}$. Instead, if it is an elongated ellipsoid it should have a bulk density $\rho \sim 650\,\mathrm{kg\,m^{-3}}$. The best Roche binary model for $2000\,GN_{171}$ is rendered in Fig. 13.

3.4. *2003 EL_{61}*

The lightcurve of $2003\,EL_{61}$ indicates a rotation period of $P = 3.9\,\mathrm{hr}$ and a lightcurve total range of $\Delta m = 0.28 \pm 0.04$ (Rabinowitz et al. 2006). The ex-

TABLE 6
$2000\,GN_{171}$ MODEL FIT.

S.F.[a]	θ[b]	q[c]	B/A[d]	C/A[d]	b/a[e]	c/a[e]	$\omega^2/(\pi G\rho)$[f]	$d/(A+a)$[g]	ρ[h]	$\chi^2/\chi^2_{\rm best}$[i]
Jacobi ellipsoid										
Lunar	90	-	0.62	0.44	-	-	0.342	-	613	1.05
Icy	90	-	0.75	0.50	-	-	0.362	-	579	1.19
Lunar	75	-	0.55	0.41	-	-	0.325	-	645	1.04
Icy	75	-	0.71	0.48	-	-	0.357	-	587	1.20
Roche binary										
Lunar	90	0.25	0.92	0.83	0.51	0.48	0.106	1.19	1972	1.09
Icy	90	0.25	0.94	0.87	0.74	0.69	0.084	1.46	2504	1.66
Lunar	75	0.34	0.89	0.81	0.45	0.42	0.108	1.09	1946	1.00
Icy	75	0.25	0.92	0.84	0.61	0.57	0.101	1.28	2067	1.05

[a] Surface type.[b] Aspect angle.[c] Mass ratio of the binary components.[d] Axis ratios of primary.[e] Axis ratios of the secondary[f] Spin (orbital) frequency of triaxial ellipsoid (binary).[g] Binary orbital separation.[h] Bulk density of the bodies (in $\mathrm{kg\,m^{-3}}$).[i] Ratio of χ^2 of model to χ^2 of best-fit model.

TABLE 7
$2003\,EL_{61}$ MODEL FIT.

S.F.[a]	θ[b]	q[c]	B/A[d]	C/A[d]	b/a[e]	c/a[e]	$\omega^2/(\pi G\rho)$[f]	$d/(A+a)$[g]	ρ[h]	$\chi^2/\chi^2_{\rm best}$[i]
Jacobi ellipsoid										
Lunar	90	-	0.80	0.52	-	-	0.367	-	2585	1.00
Icy	90	-	0.88	0.55	-	-	0.372	-	2551	1.01
Lunar	75	-	0.76	0.50	-	-	0.363	-	2611	1.02
Icy	75	-	0.86	0.54	-	-	0.371	-	2557	1.00
Roche binary										
Lunar	90	0.25	0.98	0.94	0.90	0.87	0.039	2.03	24049	6.08
Icy	90	0.25	0.99	0.97	0.96	0.94	0.019	2.65	49286	6.45
Lunar	75	0.25	0.95	0.89	0.79	0.75	0.071	1.58	13339	2.56
Icy	75	0.25	0.97	0.93	0.88	0.85	0.045	1.92	20841	2.46

[a] Surface type.[b] Aspect angle.[c] Mass ratio of the binary components.[d] Axis ratios of primary.[e] Axis ratios of the secondary[f] Spin (orbital) frequency of triaxial ellipsoid (binary).[g] Binary orbital separation.[h] Bulk density of the bodies (in $\mathrm{kg\,m^{-3}}$).[i] Ratio of χ^2 of model to χ^2 of best-fit model.

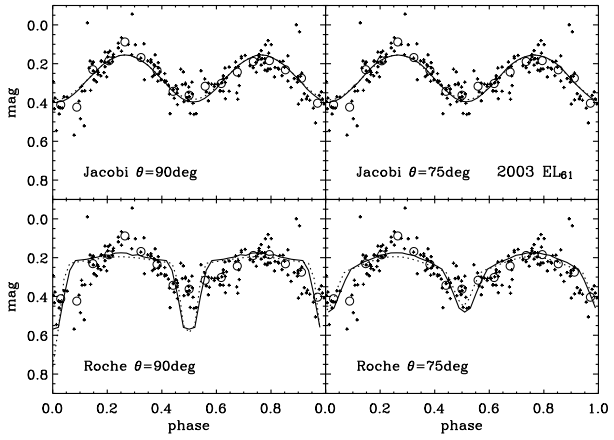

FIG. 15.— Same as Fig. 9 but for $2003\,EL_{61}$.

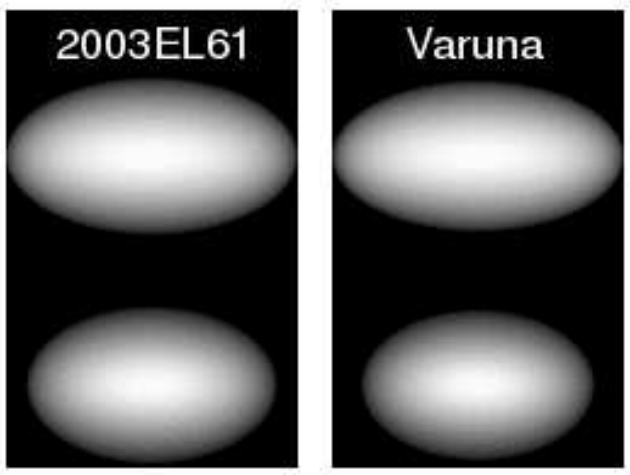

FIG. 16.— Side (top) and tip (bottom) views of the Jacobi ellipsoid models of $2003\,EL_{61}$ (left) and (20000) Varuna (right).

tremely fast rotation of $2003\,EL_{61}$ implies that it must have a high density. Using a hydrostatic equilibrium

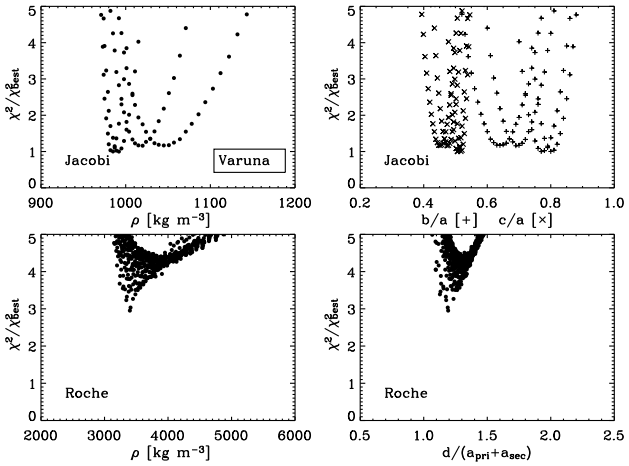

FIG. 17.— Same as Fig. 8 but for (20000) Varuna lightcurve data. Jacobi ellipsoid models are plotted for all four combinations of surface properties and observational geometry listed in Table 8, while Roche binary models are plotted for lunar-type surface and aspect angle $\theta = 75°$.

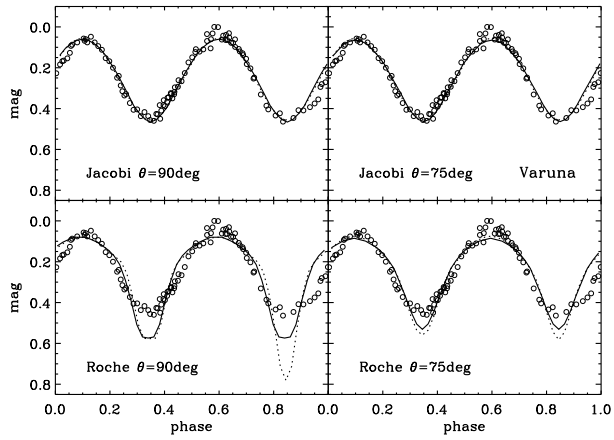

FIG. 18.— Same as Fig. 9 but for (20000) Varuna.

criterion, Rabinowitz et al. (2006) estimate $\rho \sim 2600 - 3340\,\mathrm{kg\,m^{-3}}$. A binary solution would require a considerably higher (and unrealistic) density than a rotationally deformed ellipsoid. Binarity is also unlikely given the small range of brightness variation: for a binary to produce such a shallow lightcurve, the pole axis must nearly coincide with the line of sight. Indeed, we find that no Roche binary model is able to satisfactorily fit this object's lightcurve data (see Table 7 and Fig. 14). In the case of Jacobi ellipsoid models, all possible combinations of surface properties or orientation fit the data equally well. This is partly due to the large scatter present in the lightcurve data. However, the predicted density ($\rho = 2585^{+81}_{-44}\,\mathrm{kg\,m^{-3}}$) depends little on specific choices of surface and geometry, and is consistent with the $\rho = 2600 - 3340\,\mathrm{kg\,m^{-3}}$ estimate of Rabinowitz et al. (2006). We find that the axis ratios of $2003\,\mathrm{EL_{61}}$ should fall in the ranges $b/a = 0.76 - 0.88$ and $c/a = 0.50 - 0.55$. The icy scattering law (with $\theta = 75$ deg; see Table 7) is preferable, as Rabinowitz et al. (2006) find that $2001\,\mathrm{EL_{61}}$ has a high albedo (>0.6). The best Jacobi ellipsoid representation of $2001\,\mathrm{EL_{61}}$ is shown in Fig. 16.

3.5. *(20000) Varuna*

The rotational properties of this object ($P = 6.34\,\mathrm{hr}$ and $\Delta m = 0.42 \pm 0.02$) were interpreted in the context of ellipsoidal figures of equilibrium and a density of $\rho \sim 1000\,\mathrm{kg\,m^{-3}}$ was derived (Jewitt & Sheppard 2002). Our simulations lend support to this result by showing that (20000) Varuna's lightcurve is well fit by a Jacobi ellipsoid model. This is apparent from Table 8 and Figs. 17 and 18. Figure 16 depicts the Jacobi ellipsoid model of Varuna. As in the case of $2003\,\mathrm{EL_{61}}$, the quality of fit is degenerate as far as surface properties and orientation are concerned. Thus, depending on particular choices of these properties, Varuna's axis ratios lie in the ranges $b/a = 0.63 - 0.80$, $c/a = 0.45 - 0.52$. The bulk density determination is again much more robust: we find $\rho = 992^{+86}_{-15}\,\mathrm{kg\,m^{-3}}$.

4. DISCUSSION

The photometric lightcurve of $2003\,\mathrm{EL_{61}}$ exhibits asymmetries which are not reproduced by the simple Jacobi ellipsoid model. Given the large size of this object ($D_{\mathrm{eq}} \sim 1450$, see Table 2) which safely puts it in the gravity regime, we do not expect such irregularities in the lightcurve to be due to an irregular shape. Instead, if the lightcurve features are real, they could have the same origin as Pluto's brightness variation: albedo patches across the object's surface. Like Pluto, $2003\,\mathrm{EL_{61}}$ is large enough to hold a thin atmosphere, which might condense on the surface and cause the patches.

The high density derived for (624) Hektor stands in contrast to the low value ($\rho = 800^{+200}_{-100}$ kg m^{-3}) derived for resolved Trojan binary (617) Patroclus (Marchis et al. 2006a). The sizes of these two Trojans are similar: Hektor is 102±2 km in radius while Patroclus is 70±2 km in radius, when measured and interpreted in the same way (Fernández et al. 2003). The low density of Patroclus requires substantial porosity and also suggests an ice-rich composition. Hektor's density is consistent with zero porosity and a smaller or negligible ice fraction. This difference is puzzling, given that the albedos (0.057±0.004 and 0.050±0.005, respectively) are very similar, as are the optical reflectivity gradients [11.6±1 %/1000 Å (Sawyer 1991) and 8.8±1 %/1000 Å (Jewitt & Luu 1990), respectively].

Marchis et al. (2006a) argued that the low density and inferred porous, ice-rich composition of (617) Patroclus was an indication that it originated in the outer part of the solar system. The high density of (624) Hektor is hard to explain in this context; does it indicate that (624) Hektor did not form in the outer solar system? Analogously, the similar size and surface properties of these two Jovian Trojans could be used to infer a *common* origin. A similar density argument was used for the Saturnian irregular satellite Phoebe (∼ 220 km in radius), but in the opposite direction. The *high* density of Phoebe ($\rho = 1630 \pm 33\,\mathrm{kg\,m^{-3}}$), when compared with that of other (regular) moons of Saturn, has been intepreted as indicative of an outer solar system origin on the basis that it matches the density of Pluto (Johnson & Lunine 2005). As the examples above show, it is difficult to establish a simple relation between formation region and bulk density – there may be no such relation – and therefore the density of a body alone should not be used to infer its origin.

TABLE 8
(20000) Varuna model fit.

S.F. [a]	θ [b]	q [c]	B/A [d]	C/A [d]	b/a [e]	c/a [e]	$\omega^2/(\pi G\rho)$ [f]	$d/(A+a)$ [g]	ρ [h]	$\chi^2/\chi^2_{\rm best}$ [i]
Jacobi ellipsoid										
Lunar	90	-	0.69	0.47	-	-	0.354	-	1020	1.16
Icy	90	-	0.80	0.52	-	-	0.367	-	985	1.00
Lunar	75	-	0.64	0.45	-	-	0.346	-	1045	1.17
Icy	75	-	0.77	0.51	-	-	0.364	-	992	1.00
Roche binary										
Lunar	90	0.25	0.92	0.84	0.61	0.57	0.101	1.28	3563	5.48
Icy	90	0.25	0.95	0.88	0.76	0.72	0.078	1.52	4657	8.12
Lunar	75	0.25	0.92	0.83	0.51	0.48	0.106	1.19	3399	2.95
Icy	75	0.25	0.93	0.85	0.66	0.62	0.096	1.34	3780	3.53

[a] Surface type. [b] Aspect angle. [c] Mass ratio of the binary components. [d] Axis ratios of primary. [e] Axis ratios of the secondary [f] Spin (orbital) frequency of triaxial ellipsoid (binary). [g] Binary orbital separation. [h] Bulk density of the bodies (in $\mathrm{kg\,m^{-3}}$). [i] Ratio of χ^2 of model to χ^2 of best-fit model.

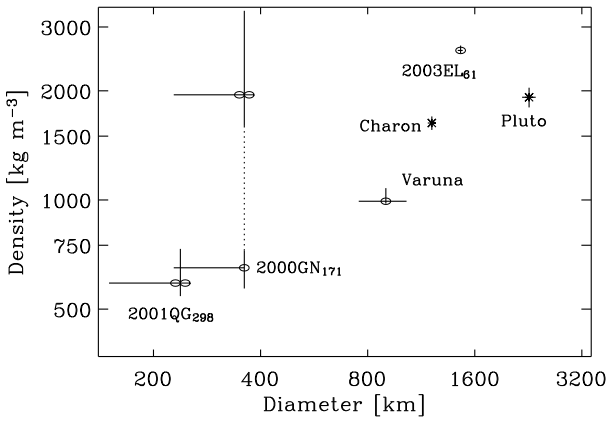

Fig. 19.— Log density versus log equivalent circular diameter for the four KBOs modeled. Jacobi ellipsoid (Roche binary) fits are indicated by single (double) ellipsoid symbols. Pluto and Charon are plotted for comparison. KBO 2000 $\mathrm{GN_{171}}$ is plotted twice (connected by a dotted line). References in the text.

Figure 19 shows the KBO densities from our simulations versus equivalent circular diameter; Pluto and Charon (Person et al. 2006) are plotted for comparison. The sizes of 2001 $\mathrm{QG_{298}}$ and 2001 $\mathrm{GN_{171}}$ were calculated from their absolute magnitude assuming a 0.04 albedo, and the error bars extend the albedo to 0.10. The size of (20000) Varuna is from Jewitt et al. (2001) and that of 2003 $\mathrm{EL_{61}}$ is calculated using its mass (Rabinowitz et al. 2006) and the density derived here (see also Table 2). A trend of increasing density with size is clear. Such relation may be caused by (1) a difference in composition (ice/rock ratio), with bigger objects having larger rock fractions, or (2) a trend in porosity, with larger objects being more compacted than their smaller counterparts, likely due to larger internal pressure. Although the latter effect is certainly present, it is unclear if it is the dominant cause for the trend. This size-density relation has been noted before (Jewitt 2002) and seems to be present in different populations, e.g., KBOs and planetary satellites (Jewitt in print).

5. THE FRACTION OF CONTACT BINARIES IN THE KUIPER BELT

Our simulations can be used to determine the lightcurve range of Roche binaries at arbitrary observing geometries, and for two different surface types. We make use of this feature to refine an earlier estimate of the contact binary fraction in the Kuiper Belt (KB; see Sheppard & Jewitt 2004). Leone et al. (1984) considered that lightcurves with ranges between 0.9 and 1.2 magnitudes must be produced by tidally deformed contact binaries (see also Weidenschilling 1980). While the maximum range of 1.2 mag is valid for lunar-type surfaces having negligible limb darkening, our simulations show that Roche binaries with icy-type surfaces (and thus significant limb darkening) can produce lightcurve ranges up to 1.57 mag. We searched our models for the binaries that produce these maximal lightcurve ranges (1.2 mag for lunar surface and 1.57 mag for icy surface) when observed equator-on, i.e., at aspect angle $\theta = 90°$. The aspect angle is measured between the line of sight and the pole axis of the binary. As the pole axis of such a binary moves away from the equator-on configuration (as the aspect angle approaches 0°) the lightcurve range becomes smaller and smaller; let us denote by $\theta_{\rm min}$ the aspect angle at which the lightcurve range reaches 0.9 mag. If we assume that the pole axes of KB contact binaries are randomly oriented in space then the detected contact binary fraction is less than the true fraction by a (geometrical correction) factor $\cos\theta_{\rm min}$.

Using our simulations we find the geometrical correction factor to be $\sim \cos(81.4°) = 0.15$ for lunar-type surfaces and $\sim \cos(70.7°) = 0.33$ for binaries with an icy-type surface (see Fig. 20). We use the fraction of 1/34 objects with large (> 0.9 mag) lightcurve range measured by Sheppard & Jewitt (2004), as it constitutes the largest homogeneous survey for variability. Therefore, considering only lunar-type surfaces the true fraction of contact binaries is $f \sim 1/(34 \times 0.15) \sim 0.20$. If we consider icy-type surfaces then we estimate the fraction to be $f \sim 1/(34 \times 0.33) \sim 0.09$. Two arguments make the latter of the two estimates a strong lower limit for the true fraction of contact (or close) KB binaries. Firstly, the two

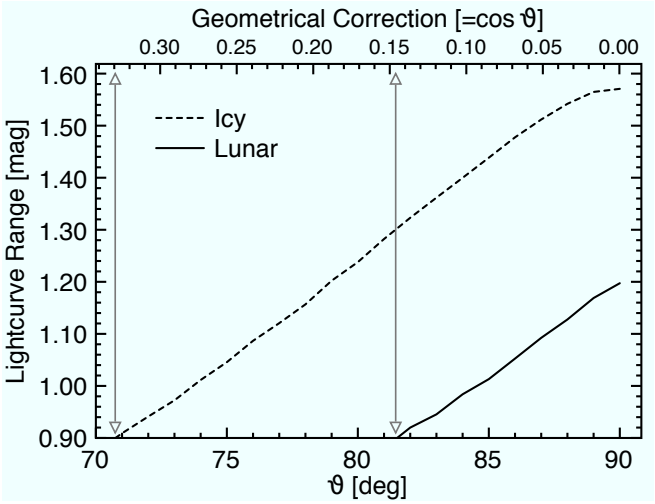

FIG. 20.— Lightcurve range as function of aspect angle θ for maximal Δm Roche binaries with both lunar- and icy-type surfaces. Top x-axis shows probability that the binary is observed at equal or larger θ. See text for details.

surface types used here are simplified limiting models of how real planetary surfaces scatter light. Real objects presumably exhibit a degree of limb darkening between the two simulated here. Secondly, contact binaries with relatively low mass ratios produce shallower lightcurves which fall below the 0.9 mag threshold adopted here, and are not accounted for. Our estimate, new in that it includes the effect of surface scattering, substantiates the idea that a considerable population of contact/close binary objects in the Kuiper Belt may await discovery (Sheppard & Jewitt 2004).

The Pan-STARRS all-sky survey (http://pan-starrs.ifa.hawaii.edu/) will scan the entire visible sky, down to $m_R \sim 24$, on a weekly basis (Kaiser & Pan-STARRS Team 2005). Besides detecting all moving objects to that brightness limit, this cadence will allow (sparsely sampled) time series photometric studies, and thus the detection of high variability candidates, suitable for follow-up observations. The survey will therefore significantly improve the estimate of the contact binary fraction. The intrinsic fraction of KB contact binaries can provide important constraints on binary formation mechanisms (e.g. Goldreich et al. 2002) and collisional evolution in the KB region (Petit & Mousis 2004).

6. SUMMARY

Mathematically unique interpretations of rotational lightcurve data are generally impossible. Nevertheless, lightcurves can, under physically plausible assumptions, convey invaluable information about the spins, shapes and densities of small solar system bodies. In this work we have explored the role of surface scattering properties on the derivation of bulk densities from rotational lightcurves, using a quantitative model of rotationally deformed bodies. We find that:

- With few exceptions, the choice of a particular scattering function does not strongly affect the densities we obtain from our simulations. Instead, the presence of surface irregularities (lumps) and some albedo variegation (spots) on the objects sets the limit to the precision of our density estimates; surface lumps and spots make it impossible to find *one* idealized equilibrium shape that matches the lightcurve, leading to some degeneracy in the fits.

- Our density estimates suggest a trend of increasing density with size. It is still unclear if such relation is mainly due to composition, to a trend in porosity, or to a combination of both.

Confirming previous inferences, we find that:

- The lightcurves of (20000) Varuna and 2003 EL_{61} are well-matched by rotational equilibrium models in which the bodies are deformed by rotation into a triaxial shape. Jacobi ellipsoid models with uniform surface albedo and a range of limb darkening functions have been used to derive the bulk densities (Varuna: $992^{+86}_{-15}\,\mathrm{kg\,m^{-3}}$; 2003 EL_{61}: $2551^{+115}_{-10}\,\mathrm{kg\,m^{-3}}$.

- The lightcurves of Jovian Trojan (624) Hektor and KBO 2001 QG_{298} are well-described by contact binary models in which the densities are $2480^{+292}_{-80}\,\mathrm{kg\,m^{-3}}$ and $590^{+143}_{-47}\,\mathrm{kg\,m^{-3}}$, respectively.

- The high incidence of KBO lightcurves consistent with a contact binary interpretation suggests that these bodies are common in the Kuiper belt.

ACKNOWLEDGMENTS

PL is grateful to the Fundação para a Ciência e a Tecnologia (BPD/SPFH/18828/2004) for financial support. This work was supported, in part, by a grant from the NSF to DCJ.

REFERENCES

Belskaya, I. N., Ortiz, J. L., Rousselot, P., Ivanova, V., Borisov, G., Shevchenko, V. G., & Peixinho, N. 2006, Icarus, 184, 277
Cellino, A., Zappala, V., & Farinella, P. 1989, Icarus, 78, 298
Chandrasekhar, S. 1963, ApJ, 138, 1182
—. 1969, Ellipsoidal figures of equilibrium (The Silliman Foundation Lectures, New Haven: Yale University Press, 1969)
Chandrasekhar, S. & Lebovitz, N. R. 1962, ApJ, 136, 1037
Cruikshank, D. P. 1977, Icarus, 30, 224
—. 2005, Advances in Space Research, 36, 1070
de Angelis, G. 1995, Planet. Space Sci., 43, 649
Degewij, J., Tedesco, E. F., & Zellner, B. 1979, Icarus, 40, 364
Dunlap, J. L. & Gehrels, T. 1969, AJ, 74, 796
Fernández, Y. R., Sheppard, S. S., & Jewitt, D. C. 2003, AJ, 126, 1563
Goldreich, P., Lithwick, Y., & Sari, R. 2002, Nature, 420, 643
Hartmann, W. K. & Cruikshank, D. P. 1978, Icarus, 36, 353
—. 1980, Science, 207, 976
Hicks, M. D., Simonelli, D. P., & Buratti, B. J. 2005, Icarus, 176, 492
Jeans, J. H. 1919, Problems of cosmogony and stellar dynamics (Cambridge, University press, 1919.)
Jewitt, D. 2002, in ESA SP-500: Asteroids, Comets, and Meteors: ACM 2002, ed. B. Warmbein, 11–19

Jewitt, D. in print, in Saas-Fee Advanced Course 35: Trans-Neptunian Objects and Comets, ed. D. Jewitt, A. Morbidelli, & H. Rauer (Springer)
Jewitt, D., Aussel, H., & Evans, A. 2001, Nature, 411, 446
Jewitt, D. C. & Luu, J. X. 1990, AJ, 100, 933
Jewitt, D. C. & Sheppard, S. S. 2002, AJ, 123, 2110
Johnson, T. V. & Lunine, J. I. 2005, Nature, 435, 69
Kaasalainen, M., Mottola, S., & Fulchignoni, M. 2002, Asteroids III, 139
Kaasalainen, M. & Torppa, J. 2001, Icarus, 153, 24
Kaasalainen, M., Torppa, J., & Muinonen, K. 2001, Icarus, 153, 37
Kaiser, N. & Pan-STARRS Team. 2005, Bulletin of the American Astronomical Society, 37, 1409
Leone, G., Paolicchi, P., Farinella, P., & Zappala, V. 1984, A&A, 140, 265
Li, J.-Y. 2005, Ph.D. Thesis
Marchis, F., Hestroffer, D., Descamps, P., Berthier, J., Bouchez, A. H., Campbell, R. D., Chin, J. C. Y., van Dam, M. A., Hartman, S. K., Johansson, E. M., Lafon, R. E., Le Mignant, D., de Pater, I., Stomski, P. J., Summers, D. M., Vachier, F., Wizinovich, P. L., & Wong, M. H. 2006a, Nature, 439, 565
Marchis, F., Wong, M. H., Berthier, J., Descamps, P., Hestroffer, D., Vachier, F., Le Mignant, D., Keck Observatory, W. M., & de Pater, I. 2006b, IAU Circ., 8732, 1
Millis, R. L. 1977, Icarus, 31, 81
Person, M. J., Elliot, J. L., Gulbis, A. A. S., Pasachoff, J. M., Babcock, B. A., Souza, S. P., & Gangestad, J. W. 2006, AJ, 132, 1575
Petit, J.-M. & Mousis, O. 2004, Icarus, 168, 409
Rabinowitz, D. L., Barkume, K., Brown, M. E., Roe, H., Schwartz, M., Tourtellotte, S., & Trujillo, C. 2006, ApJ, 639, 1238
Russell, H. N. 1906, ApJ, 24, 1
Sawyer, S. R. 1991, Ph.D. Thesis
Sheppard, S. S. & Jewitt, D. 2004, AJ, 127, 3023
Sheppard, S. S. & Jewitt, D. C. 2002, AJ, 124, 1757
Takahashi, S. & Ip, W.-H. 2004, PASJ, 56, 1099
Weidenschilling, S. J. 1980, Icarus, 44, 807
Wijesinghe, M. P. & Tedesco, E. F. 1979, Icarus, 40, 383